THE JOURNAL OF PHYSICAL CHEMISTRY Letters

pubs.acs.org/JPCL Letter

Hot Carrier Cooling and Recombination Dynamics of Chlorine-Doped Hybrid Perovskite Single Crystals

L. Tyler Mix,* Dibyajyoti Ghosh, Jeremy Tisdale, Min-Cheol Lee, Kenneth R. O'Neal, Nicholas Sirica, Amanda J. Neukirch, Wanyi Nie, Antoinette J. Taylor, Rohit P. Prasankumar, Sergei Tretiak, and Dmitry A. Yarotski*

Cite This: J. Phys. Chem. Lett. 2020, 11, 8430–8436 Read Online

ACCESS | Metrics & More | Article Recommendations | Supporting Information

ABSTRACT: Controlling the photoexcited properties and behavior of hybrid perovskites by halide doping has the potential to impact a wide range of emerging technologies, including solar cells and radiation detectors. Crystalline samples of methylammonium lead bromide substituted with chlorine ($MAPbBr_{3-x}Cl_x$) were examined by transient reflectivity spectroscopy and nonadiabatic molecular dynamics simulations. At picosecond time scales, the addition of chlorine to the perovskite crystal increased the observed rate of hot carrier cooling and the calculated electron–phonon coupling constants. Chlorine-doped samples also exhibit a slower surface recombination velocity and a smaller ambipolar mobility.

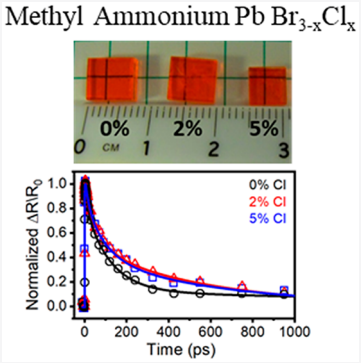

Hybrid organic–inorganic perovskites (HOIP) have emerged as a potential rival to silicon as the semiconductor of choice in optoelectronic applications.[1−3] HOIP rose to prominence due to their rapidly improving performance as photovoltaic solar cells, demonstrating similar efficiencies to conventional Si and GaAs semiconductors.[1−3] Currently, hybrid perovskites are in the early stages of development for other possible uses such as thin film transistors,[4,5] photodetectors,[6] radiation detectors,[7,8] optical gain media,[9] and light emitting devices.[10−12] Improving and optimizing HOIP to efficiently control energy and charge generation and transfer for technological applications requires a detailed understanding of the interplay between chemical composition, electronic structure, and optical properties.

The most common HOIPs are methylammonium lead halides ($MAPbX_3$), which are formed by a lead halide anion $[PbX_6]^{4-}$ (X = Cl, Br, or I) placed in an octahedral network stabilized by a methylammonium (MA) cation $[CH_3NH_3]^+$ at the center of the octahedra.[13,14] $MAPbX_3$ is a direct gap semiconductor that exhibits sharp band edge absorption and strong photoluminescence. Halide substitution or alloying has a significant impact on the electronic structure and photophysical properties,[15,16] as these ions make a large contribution to the valence band structure.[17,18] For example, chlorine doping in $MAPbBr_3$ during testing of γ-radiation detectors shows improvement in the sensitivity and spectral resolution of γ-ray detection.[19] The mechanisms of this enhancement are still poorly understood, despite their importance for the development of γ-ray detectors with enhanced performance and reduced cost.

Here, we investigate the hot carrier cooling and surface recombination dynamics of $MAPbBr_{3-x}Cl_x$ single crystals. These processes are critical in enabling the enhanced electronic transport and charge collection found in photovoltaic devices based on these materials. Rapid hot carrier cooling, mediated by electron–phonon coupling, prevents carrier trapping and promotes radiative relaxation and has been shown to improve performance in light emitting devices.[20] High surface carrier recombination rates lead to unfavorable performance in many HOIP devices, as the photocarriers are quenched before they can be separated and collected.[21] In this work, we combine ultrafast optical measurements with first-principles calculations to demonstrate that a small percentage of Cl substitution in $MAPbBr_3$ crystals leads to significantly faster carrier cooling dynamics and lower surface recombination rates, which may be responsible for the observed improvement in the performance of high-energy radiation detectors and other optoelectronic devices.

Received: July 22, 2020
Accepted: September 9, 2020
Published: September 9, 2020

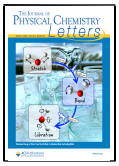

https://dx.doi.org/10.1021/acs.jpclett.0c02243
J. Phys. Chem. Lett. 2020, 11, 8430–8436

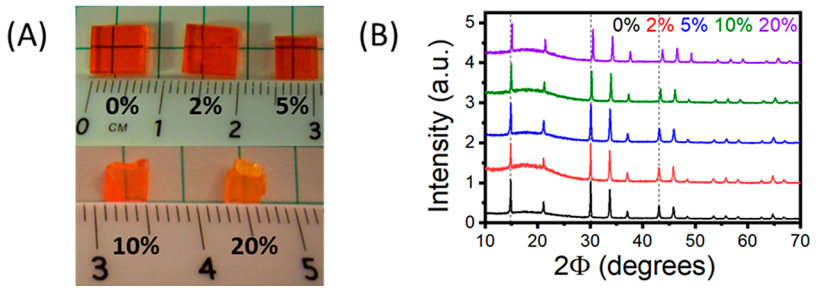

Figure 1. (A) Pictures of $MAPbBr_{3-x}Cl_x$ single crystals, where x = 0, 0.06, 0.15, 0.30, 0.60. (B) X-ray powder diffraction results. Vertical dashed lines are a guide to illustrate the slight peak shift to large angles for increased doping.

$MAPbBr_{3-x}Cl_x$ single crystals were grown using the inverse temperature crystallization growth method.[22] Crystals were doped with Cl with x = 0 (0%), 0.06 (2%), 0.15 (5%), 0.30 (10%), and 0.60 (20%) and grown to about 5 × 5 × 2 mm^3, as shown in Figure 1A. Powder X-ray diffraction patterns for each composition are shown in Figure 1B. We observe a slight shift in peak position toward larger angles showing a decrease in the lattice parameter when increasing the doping amount of Cl. The calculated lattice parameter decreases from 5.92 Å in $MAPbBr_3$ to 5.85 Å in $MAPbBr_{2.4}Cl_{0.60}$ (20%) as expected when the smaller Cl are substituted. In previous work, we have deeply investigated absorption and photoluminescence characterizations of Cl-doped $MAPbBr_3$.[19] Absorption and photoluminescence spectra of $MAPbBr_{3-x}Cl_x$ samples show the onset of absorption increasing in photon energy as the doping percentage is increased similar to $MAPbI_{3-x}Br_x$.[19] The band gaps are 2.14, 2.17, and 2.19 eV for the undoped, 2% Cl, and 5% Cl doped samples, respectively. Higher percentages of Cl doping, which could not be measured by pump−probe spectroscopy due to increased nonuniformity and light scattering, further raise the band gap to 2.25 and 2.34 eV at 10% and 20% Cl, respectively. Computational results for the mixed anion perovskites match reasonably well to the experimental band gap measurements (Figure S1). $MAPbBr_3$ is a direct gap semiconductor where the valence band is mainly composed of halide p orbitals with small contributions from the Pb 6s orbitals and the conduction band is mostly composed of nonbonding Pb 6p orbitals with small contributions from the halide p orbitals (Figure S2).[17,18]

To observe the effects of Cl doping on the photodynamics of $MAPbBr_{3-x}Cl_x$, the transient reflectivities of three samples, x = 0 (0%), 0.06 (2%), and 0.15 (5%), were measured using femtosecond (fs) degenerate pump−probe spectroscopy at 400 nm (10 nm fwhm). All single crystals demonstrated an increase in reflectivity immediately after the pump pulse, due to the pump induced change in the refractive index as electrons that are excited into the conduction band decrease the absorption coefficient.[21] Figure 2 shows measured reflectivity transients ($\Delta R/R$) from our samples, with an initial ultrafast rise over the first few picoseconds, followed by a long decay which persists past our measurement limit of 1 ns. The pristine sample has a longer initial rise (Figure 2B) and faster decay dynamics (Figure 2A) than that of the 2% and 5% Cl-doped samples.

Reflectivity transients do not show any significant pump fluence dependence between 19 and 39 $\mu J/cm^2$ besides the expected linear change of the total signal amplitude (Figure 2C), as similarly observed by Beard and co-workers with undoped $MAPbBr_3$ crystals.[21] The rising component is

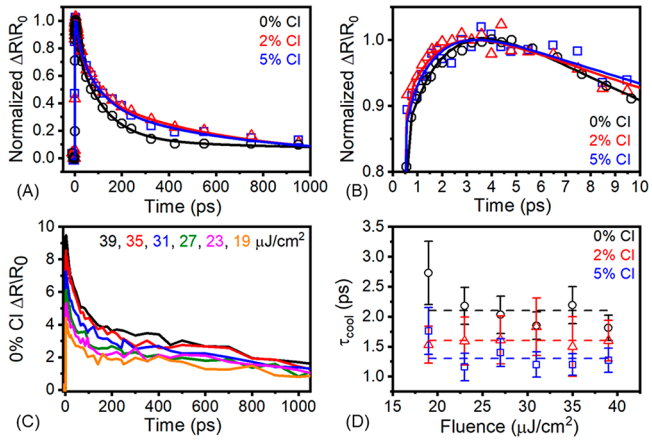

Figure 2. Measured reflectivity transients. Normalized and averaged transients (symbols) with exponential fits (lines) show the pristine sample has the fastest decay dynamics (A) while those in the doped samples are slower and are very similar to one another. In contrast, the pristine sample has the slowest rise dynamics, while the 5% Cl sample has the fastest (B). Energy fluence-dependent measurements (C) of the 0% sample. Doping dependence of the rise time, τ_{cool}, from exponential fits (D) of reflectivity transients with the average (over all energy fluences), τ_{cool}, shown by the dotted line. There is no clear excitation fluence dependence of τ_{cool} for each Cl doping level. Increases in Cl doping percentage are concomitant to decreases in τ_{cool}.

attributed to a hot carrier cooling process that occurs after the dissociation of excitons and formation of free carriers in ∼100 fs.[23] The reflectivity increases as the hot electrons relax to the bottom of the conduction band nonradiatively by scattering and thermalization with phonons.[24] The decaying component is attributed to surface recombination of the excited electrons back to the valence band and diffusion of the carriers out of the probe volume (30 μm diameter with ∼100 nm penetration depth) and into the bulk.[21] Radiative first-order recombination effects are not considered here because photoluminescence occurs on a much longer time scale of ∼30 ns.[21]

Reflectivity transients were first fitted with an exponential model incorporating a rising component and three decaying components (Supporting Information, Eq 1). Figure 2D shows the comparison of the time constant, τ_{cool}, for the rising component at different pump fluences. The general trend is toward faster cooling with increased Cl doping. The rising component, τ_{cool}, for pristine $MAPbBr_3$ is 2.1 ± 0.15 ps, 1.6 ± 0.2 ps for $MAPbCl_{0.06}Br_{2.94}$, and 1.3 ± 0.2 ps for $MAPbCl_{0.15}Br_{2.85}$. Cooling of hot carriers in $MAPbBr_{3-x}Cl_x$ perovskites, $\tau_{cool} \approx$ 1.5 ps, is a few times slower than that of

https://dx.doi.org/10.1021/acs.jpclett.0c02243
J. Phys. Chem. Lett. 2020, 11, 8430−8436

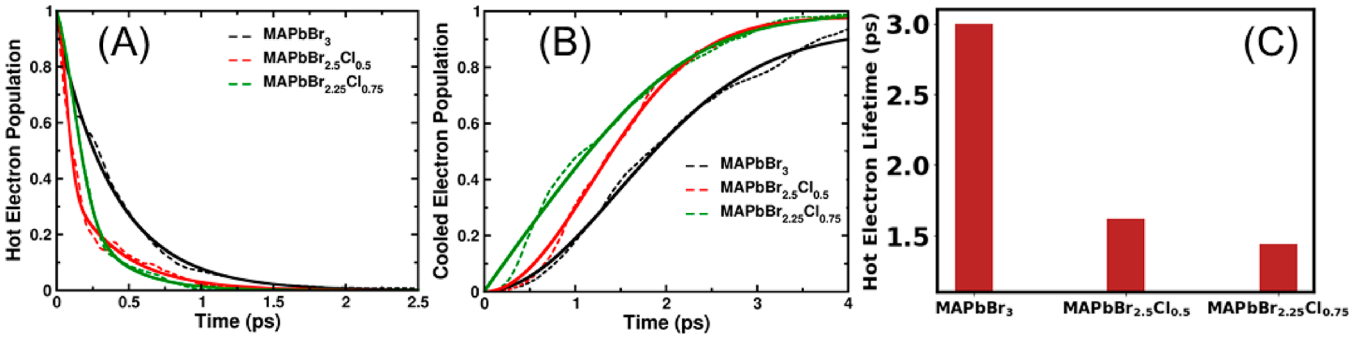

Figure 3. Simulated temporal evolution of (A) hot electron populations in CBM+7 and in the (B) band edge states, CBM and CBM+1, (see Supporting Information section S1 for details) of $MAPbBr_3$, $MAPbBr_{2.5}Cl_{0.5}$, and $MAPbBr_{2.25}Cl_{0.75}$. Solid lines represent the fitted time evolution of the populations, according to Supporting Information Eqs 3 and 5. The faster increase in the cooled electron population for $MAPbBr_{3-x}Cl_x$ lattices indicates faster electron cooling with anion mixing. (C) Calculated hot electron lifetimes of $MAPbBr_{3-x}Cl_x$, as detailed in section S2, Supporting Information. The lifetime decreases with Cl doping in bromide perovskites.

GaAs, $\tau_{cool} \approx 0.5$ ps,[25] slower than $MAPbI_3$ nanocrystals, $\tau_{cool} \approx 0.5$ ps,[26] and slower than $MaPbI_3$ thin films, $\tau_{cool} \approx 0.6$ ps.[27] The cause of the slower cooling rate compared to $MAPbI_3$ experiments is a matter for future investigation. An initial hypothesis is that fewer defects present in the single crystals used in these experiments versus thin films and nanocrystals, would affect the rate as these faster rates were proscribed to the activation of traps when carriers are far above the band gap.[26] Further experiments with improved white light probing or a three-pulse pump−push−probe sequence could provide increased accuracy to the hot carrier cooling rates. The exact details of carrier cooling in $MAPbBr_{3-x}Cl_x$ are under continuing investigation, but faster carrier cooling with substitution of a lighter halide agrees with calculations (discussed below) and previous studies of the all-inorganic perovskite $CsPbBr_3$.[20]

The observed rise times do not display a clear dependence on the pump fluence (Figure 2D), and the variation in τ_{cool} can be attributed to small sample inhomogeneity as the crystal is moved to a new spot for each fluence measurement. A phonon bottleneck limiting the decay from optical phonons into acoustic phonons has been shown to slow carrier cooling in $MAPbI_3$, with $\tau_{cool} \approx 75$ ps, under intense excitation as carrier density increases. No observed fluence dependence indicates that the hot carrier phonon bottleneck effect in single crystal $MAPbBr_3$ is either not present or much smaller than observed in $MAPbI_3$ thin films.[25]

To deepen the understanding of the influence of Cl doping on carrier cooling, we performed Nonadiabatic Molecular Dynamics (NAMD) simulations on $MAPbBr_3$ and $MAPbBr_{3-x}Cl_x$ (x = 0.50, 0.75) lattices (Supporting Information section S1B). To model the hot carrier cooling processes, we studied the relaxation of both types of carriers: electrons relaxing to the conduction band minimum (CBM) and holes relaxing to the valence band maximum (VBM). We calculated the populations of carriers in the initially excited states and band edge states. The dynamical population and depopulation rates of these states are directly related to the carrier relaxation processes after excitation. The decreased population of the initially excited state and increased population at the band edges over the simulation times demonstrate the carrier cooling from high energy states to the VBM/CBM following photoexcitation. A faster decrease in the population of the excited state or a faster increase of the population of the VBM/CBM corresponds to a faster carrier cooling process.

To model the hot-electron cooling process, we initially populate the seventh electronic state above the CBM, or CBM +7, which is ∼3.1 eV above the VBM, to mimic the 3.1 eV pump laser in the transient reflectivity experiments (Supporting Information section S1B). Within hundreds of femtoseconds the hot electrons depopulate the highest excited state (Figure 3A) and start accumulating in the conduction band edge states (Figure 3B). In pristine $MAPbBr_3$, half of the excited electron population has relaxed to the band edge states within the first 1.86 ps (Figure 3B). The hot-electron relaxation from the highest excited state to the conduction band edge becomes faster with Cl incorporation in $MAPbBr_{3-x}Cl_x$. Half of the excited electron population has relaxed to the band edge within the first 1.39 and 1.11 ps for $MAPbBr_{2.5}Cl_{0.5}$ and $MAPbBr_{2.25}Cl_{0.75}$, respectively. Almost 100% of hot electrons in mixed halide perovskites cool down to the conduction band edge states within the considered time scale, 4 ps. However, for pristine $MAPbBr_3$, a fraction of hot electrons (∼8%) still remain in the excited states after 4 ps, depicting a slower cooling process compared to mixed halide samples.

Fitting the population curves with a sum of exponential and Gaussian functions[28] (Supporting Information section S2), we estimate the hot electron lifetime for $MAPbBr_3$ to be 3.0 ps, which reduces to 1.62 and 1.44 ps for $MAPbBr_{2.5}Cl_{0.5}$ and $MAPbBr_{2.25}Cl_{0.75}$, respectively (Figure 3C and Table S1). Within the Cl doping limit considered here, we find up to ∼2 times faster hot electron cooling in $MAPbBr_{3-x}Cl_x$ compared to $MAPbBr_3$. Additionally, the decrease in the electron population at the highest excited state (Figure 3A, dashed and solid red lines) shows faster decay of hot carriers with anion mixing. This further supports the quicker carrier cooling process in $MAPbBr_{3-x}Cl_x$ lattices. Note that we cannot quantitatively compare the relative change in the computed carrier lifetimes with the experimentally calculated rise times, as the Cl doping concentrations are much higher for computational models compared to experimental samples. Nevertheless, the trend of hot electron lifetimes is consistent for both theoretical and experimental investigations.

We also calculated the relaxation of the excess electron energy (∼0.9 eV) deposited by photoexcitation above the conduction band edge. All the systems considered here have a similar distribution of energy states in the conduction and

https://dx.doi.org/10.1021/acs.jpclett.0c02243
J. Phys. Chem. Lett. 2020, 11, 8430−8436

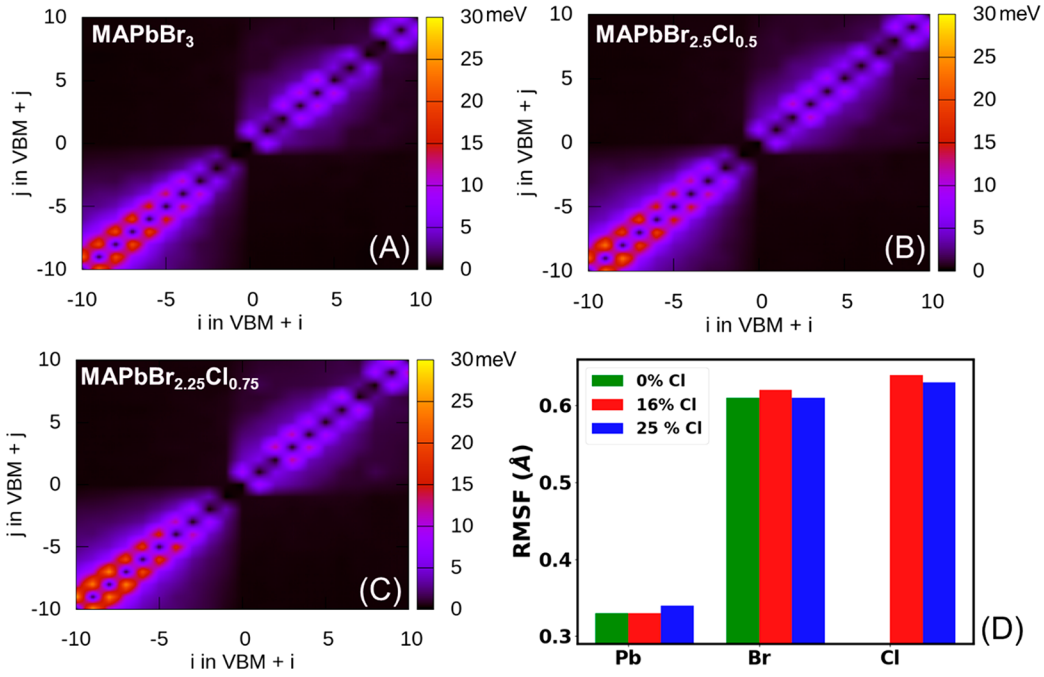

Figure 4. Time-averaged magnitude of the carrier-phonon NACs in valence and conduction bands for (A) $MAPbBr_3$, (B) $MAPbBr_{2.5}Cl_{0.5}$, and (C) $MAPbBr_{2.25}Cl_{0.75}$. In these plots, $i = 0$ is the VBM, negative values are other lower valence states, and positive values relate to conduction band states. $MAPbBr_{3-x}Cl_x$ lattices exhibit higher NACs compared to MAPbBr. (D) Root-mean-square fluctuations (RMSF) of inorganic atoms in the perovskite lattices.

valence bands (Figure S3). The excess energy dissipates faster (Figure S4) in $MAPbBr_{3-x}Cl_x$ compared to $MAPbBr_3$, supporting the hot electron cooling trend. As the number of involved electronic states in the cooling process is the same for pristine and mixed-anion perovskites (Figure S3), we understand that the faster cooling in $MAPbBr_{3-x}Cl_x$ originates from the stronger effective electron−phonon interaction in doped lattices.

We further model the relaxation of hot holes that are created deep in the valence band to the VBM. Simulated hot hole dynamics reveal that these carriers decay at a much faster rate than hot electrons (Figure S5). Half of the excited holes had relaxed to the valence band edge within ∼0.66−0.75 ps following the excitation (Figure S5) in $MAPbBr_{3-x}Cl_x$. Fast cooling of hot holes make these carriers less important for hot carrier harvesting in halide perovskites.

To understand the influence of anions on the carrier cooling rates in $MAPbBr_{3-x}Cl_x$ at the microscopic level, we calculate the nonadiabatic couplings (NACs) between the participating electronic states in both valence and conduction bands. Higher NAC values mean stronger hot carrier−phonon interactions, leading to faster cooling of the carriers. We plot the absolute NAC values averaged over 4 ps of *ab initio* molecular dynamics trajectories in Figure 4A−C. The higher coupling values along the subdiagonal line indicate that energetically adjacent electronic states dominate the nonradiative transitions during the carrier cooling process. Direct multiphonon transitions between energetically nonadjacent states are possible due to nonzero NAC values, the purple halo around the strong diagonals; however, these transitions are much weaker compared to sequential transfers between energetically adjacent states.

The NAC values in the valence bands ($i < 0$, Figure 4A−C) are considerably higher compared to the coupling values for the conduction band states ($i \geq 1$, Figure 4A−C). This explains the faster cooling of hot holes compared to hot electrons in all the $MAPbBr_{3-x}Cl_x$. The much higher density of states (DOS) in the valence bands gives rise to the stronger NAC values compared to that in the conduction bands (Figure S2). The average NAC values for electrons between states near the conduction band edges are 6.9, 7.8, and 8.4 meV for $MAPbBr_3$, $MAPbBr_{2.5}Cl_{0.5}$, and $MAPbBr_{2.25}Cl_{0.75}$, respectively. Holes at the valence band edges follow the same trend, with average NAC values of 8.6, 9.7, and 10.0 meV for $MAPbBr_3$, $MAPbBr_{2.5}Cl_{0.5}$, and $MAPbBr_{2.25}Cl_{0.75}$, respectively. Thus, Cl doping increases the strength of the NACs in both conduction and valence bands near the band edges (Figure 4B,C) and causes the accelerated hot electron cooling in Br-based perovskites (Figures 2 and 3). As the wave functions of states near the band edges are localized on the inorganic framework (Figure S1), changes in their structural dynamics influence the carrier cooling process by modifying the hot carrier−phonon interaction. More structural fluctuations generally give rise to higher NACs.

To find out the effects of Cl doping on structural dynamics at ambient conditions, we calculate the root-mean-square fluctuations (RMSF) of the atomic positions from *ab initio* molecular dynamics trajectories (Figure 4D). The heavy Pb fluctuates much less compared to Br/Cl atoms. Due to the lighter weight, the RMSFs of Cl are higher, ∼0.64 Å compared to ∼0.60 Å for Br. Further, increased fluctuations at the halide sites make the entire inorganic framework more dynamically active in anion mixed perovskites. Thus, incorporation of Cl atoms induces more structural fluctuations in $MAPbBr_{3-x}Cl_x$ at room temperature than in pristine samples. Enhanced structural dynamics strengthens the phonon−carrier interaction, consequently producing higher NACs in $MAPbBr_{3-x}Cl_x$. Thus, stronger lattice fluctuations make hot carrier relaxation quicker in mixed halide perovskites. It is not obvious that the NAC values follow the same increasing trend

https://dx.doi.org/10.1021/acs.jpclett.0c02243
J. Phys. Chem. Lett. 2020, 11, 8430−8436

for both valence and conduction bands with anion mixing in $MAPbBr_{3-x}Cl_x$, as the valence band is mainly composed of halide p orbitals and the conduction band is mostly composed of nonbonding Pb 6p orbitals. For valence band states, the relevant atomic sites are halides, and higher NAC values arise due to the stronger lattice fluctuations in these Br/Cl sites. For conduction bands, states formed mostly by Pb orbitals become slightly more dynamic with Cl incorporation in the lattice, as we find from the RMSF plot (Figure 4D). This higher fluctuation of Pb atoms results in increased NAC values in the conduction bands with increased Cl concentration.

Both our calculations and our pump−probe measurements show that at early times in the photodynamics of $MAPbBr_{3-x}Cl_x$ perovskites, Cl doping increases the hot carrier cooling rates and the electron−phonon coupling. Cl doping leads to band gap broadening, altering the electron and phonon states, and introducing larger structural fluctuations. More structural fluctuations in turn increase the carrier-phonon NAC in both the valence and conduction bands, which ultimately result in the observed faster hot carrier cooling.

In addition to the increase in carrier-phonon NAC with Cl doping, carrier−carrier interactions could influence the hot electron cooling rates; however, there is little evidence these processes are significant contributors in these experiments. Previous experiments on thin films of $MAPbI_3$[29] and the inorganic perovskite $CsPbBr_3$[30] illustrate that cooling rates depend on the carrier concentration with higher carrier densities, leading to faster cooling. In a mixed halide perovskite ion segregation could lead to locations with higher carrier densities and thus faster cooling. Transient reflectivity measurements at different locations on the crystal and different pump fluences (Figure 2D) do not show a noticeable dependence of τ_{cool} on fluence or location that we would expect if ion segregation or carrier−carrier interactions were prominent. Carrier−carrier interactions in these measurements of large single crystals at ∼30 $\mu J/cm^2$ are possibly a minor secondary effect and the primary driver of the faster carrier cooling rates is the increased carrier−phonon NAC with Cl doping.

To understand the long time decay of the observed transient reflectivity (Figure 2A) and the carrier recombination dynamics, we used a model that relates the reflectivity signal that is proportional to carrier density to the surface recombination velocity and the diffusion velocity (Supporting Information Eq 4).[21] Because the penetration depth into $MAPbBr_3$ of 400 nm light is ∼100 nm in transient reflectivity experiments, our signal decay is primarily the result of surface recombination and carriers diffusing away from the surface and out of the probe volume. Carriers that diffuse into the bulk and then recombine using the slower bulk recombination or fluorescence pathways, are not relevant to our signal, as these processes occur outside of our probe volume and at much slower rates than the 1 ns time window of our experiment. Without an applied bias the electrons will diffuse faster than the holes allowing us to neglect the hole diffusion to a reasonable approximation, so only a single diffusion rate is included.[21,31] This model was previously used by Beard and co-workers in similar transient reflectivity measurements on undoped $MAPbBr_3$ crystals.[21]

Fits of the pure $MAPbBr_3$ sample yield $S = (2.0 \pm 0.4) \times 10^4$ cm/s and $D = 0.16 \pm 0.01$ cm^2/s (Table 1). In line with the slower decay in the raw data, the doped samples have fitting parameters with a slower recombination velocity, where $S = (1.2 \pm 0.2) \times 10^4$ and $(1.4 \pm 0.3) \times 10^4$ cm/s and $D = 0.15 \pm 0.03$ and 0.12 ± 0.05 cm^2/s for 2% Cl and 5% Cl, respectively. The ambipolar mobility calculated with the Einstein relation is 6.2 $cm^2\ V^{-1}\ s^{-1}$ for pure $MAPbBr_3$, 5.8 $cm^2\ V^{-1}\ s^{-1}$ for 2% Cl, and 4.7 $cm^2\ V^{-1}\ s^{-1}$ for 5% Cl.

Table 1. Surface Carrier Recombination and Diffusion Model Fit Parameters

doping percentage of Cl (%)	surface recombination velocity S (cm s^{-1})	diffusion coefficient D ($cm^2\ s^{-1}$)	ambipolar mobility μ ($cm^2\ V^{-1}\ s^{-1}$)
0	$(2.0 \pm 0.4) \times 10^4$	0.16 ± 0.01	6.23
2	$(1.2 \pm 0.2) \times 10^4$	0.15 ± 0.03	5.84
5	$(1.4 \pm 0.3) \times 10^4$	0.12 ± 0.05	4.67

Our doped perovskite samples have surface recombination velocities (∼1.5×10^4 cm s^{-1}, Table 1) of up to 2 orders of magnitude slower than that of typical inorganic semiconductors before passivation: GaAs (8.5×10^5 cm s^{-1}),[32] GaP (2×10^6 cm s^{-1}),[33] p-Si (2.4×10^5 cm s^{-1}), and n-Si (1.2×10^6 cm s^{-1}).[34] This value is also an order of magnitude lower than that observed previously for pure $MAPbBr_3$ (3.4×10^3 cm s^{-1})[21] using transient reflection spectroscopy with multiple excitation wavelengths and white light probing. Surface recombination is mediated by states formed in the band gap by surface defects in the crystalline lattice. Previous calculations by Yan and co-workers[35] predict that the defects present in $MAPbX_3$ materials form fewer midgap states than in inorganic semiconductors, which may explain the low surface recombination velocities here. The introduction of Cl into $MAPbBr_3$ further slows the surface recombination velocity, implying fewer midgap states.[36] Slow recombination rates are excellent properties for photovoltaic and detector applications, as carriers are able to diffuse and be collected by the electrodes before recombination. Any carrier that recombines is not contributing charge to the detector or solar cell, thus reducing the device efficiency. We believe that the slower surface recombination velocity of Cl-doped perovskite is mainly responsible for their improved performance as radiation detectors.[19]

The diffusion coefficient (0.15 $cm^2\ s^{-1}$, Table 1) and the ambipolar mobility (∼5 $cm^2\ V^{-1}\ s^{-1}$, Table 1) observed in our experiments are smaller than that extracted from time-of-flight measurements (∼115 $cm^2\ V^{-1}\ s^{-1}$),[37] from Hall effect measurements (20 $cm^2\ V^{-1}\ s^{-1}$),[37] and from the work of Beard and co-workers (10.8 $cm^2\ V^{-1}\ s^{-1}$).[21] Ambipolar mobility for typical inorganic semiconductors are also 4 times larger, e.g., 20 $cm^2\ V^{-1}\ s^{-1}$ in GaAs[38] and 19 $cm^2\ V^{-1}\ s^{-1}$ in α-Si.[39] The introduction of Cl into the crystal lattice further impedes the diffusion of carriers (Table 1) by introducing trap states in the conduction band. These trap states must be formed above the band gap and inside the conduction band, since if they were within the gap the recombination rates would increase. Decreased diffusion coefficients are a detriment to photovoltaic and detector performance, as the carriers cannot travel to the collecting electrodes as fast and may be lost due to recombination. However, this effect can be balanced or overcome by slower recombination rates or by macroscopic means, such as placing the collection electrodes closer together.

To conclude, similar to common inorganic semiconductors, we have shown that doping single crystals of hybrid inorganic $MAPbBr_3$ perovskites with Cl can be used to control their

https://dx.doi.org/10.1021/acs.jpclett.0c02243
J. Phys. Chem. Lett. 2020, 11, 8430−8436

properties, such as diffusion and hot carrier cooling rates. Transient reflectivity experiments demonstrate that increased Cl doping enhances hot carrier cooling rates, decreases surface recombination rates, and decreases the ambipolar mobility. Calculations rationalize and support experimental transient reflectivity results, predicting that increased levels of Cl doping strengthen nonadiabatic electron−phonon coupling constants which increase the observed hot carrier cooling rates. Our results have implications for continued improvements of $MAPbX_3$ HOIP through controlled tuning of chemical doping parameters in order to enhance various photophysical properties related to performance in light emitting diodes, photovoltaics, and radiation detectors.

■ ASSOCIATED CONTENT

Supporting Information

The Supporting Information is available free of charge at https://pubs.acs.org/doi/10.1021/acs.jpclett.0c02243.

Experimental and computational details, fitting functions, table of parameters to fit the population increment, and figures of bandgap variation vs Cl doping, PDOS, Kohn−Sham orbital energies, effect of Cl doping on the excess energy dissipation, and hot hole dynamics (PDF)

■ AUTHOR INFORMATION

Corresponding Authors

L. Tyler Mix − *Center for Integrated Nanotechnologies, Los Alamos National Laboratory, Los Alamos, New Mexico 87545, United States;* orcid.org/0000-0002-8136-3457; Email: ltmix@lanl.gov

Dmitry A. Yarotski − *Center for Integrated Nanotechnologies, Los Alamos National Laboratory, Los Alamos, New Mexico 87545, United States*; Email: dzmitry@lanl.gov

Authors

Dibyajyoti Ghosh − *Theoretical Division and Center for Nonlinear Studies, Los Alamos National Laboratory, Los Alamos, New Mexico 87545, United States;* orcid.org/0000-0002-3640-7537

Jeremy Tisdale − *Material Physics and Applications Division, Los Alamos National Laboratory, Los Alamos, New Mexico 87545, United States*

Min-Cheol Lee − *Center for Integrated Nanotechnologies, Los Alamos National Laboratory, Los Alamos, New Mexico 87545, United States*

Kenneth R. O'Neal − *Center for Integrated Nanotechnologies, Los Alamos National Laboratory, Los Alamos, New Mexico 87545, United States;* orcid.org/0000-0001-9149-1957

Nicholas Sirica − *Center for Integrated Nanotechnologies, Los Alamos National Laboratory, Los Alamos, New Mexico 87545, United States*

Amanda J. Neukirch − *Theoretical Division, Los Alamos National Laboratory, Los Alamos, New Mexico 87545, United States;* orcid.org/0000-0002-6583-0086

Wanyi Nie − *Center for Nonlinear Studies, Los Alamos National Laboratory, Los Alamos, New Mexico 87545, United States;* orcid.org/0000-0002-5909-3155

Antoinette J. Taylor − *Center for Integrated Nanotechnologies, Los Alamos National Laboratory, Los Alamos, New Mexico 87545, United States*

Rohit P. Prasankumar − *Center for Integrated Nanotechnologies, Los Alamos National Laboratory, Los Alamos, New Mexico 87545, United States;* orcid.org/0000-0003-0902-2831

Sergei Tretiak − *Center for Integrated Nanotechnologies, Theoretical Division, and Center for Nonlinear Studies, Los Alamos National Laboratory, Los Alamos, New Mexico 87545, United States;* orcid.org/0000-0001-5547-3647

Complete contact information is available at: https://pubs.acs.org/10.1021/acs.jpclett.0c02243

Notes

The authors declare no competing financial interest.

■ ACKNOWLEDGMENTS

Research presented in this article was supported by the Laboratory Directed Research and Development program of Los Alamos National Laboratory. This work was performed, in part, at the Center for Integrated Nanotechnologies, an Office of Science User Facility operated for the U.S. Department of Energy (DOE) Office of Science. Los Alamos National Laboratory, an affirmative action equal opportunity employer, is managed by Triad National Security, LLC for the U.S. Department of Energy's NNSA, under contract 89233218CNA000001.

■ REFERENCES

(1) Petrović, M.; Chellappan, V.; Ramakrishna, S. Perovskites: Solar cells & engineering applications − materials and device developments. *Sol. Energy* **2015**, *122*, 678−699.

(2) Jena, A. K.; Kulkarni, A.; Miyasaka, T. Halide Perovskite Photovoltaics: Background, Status, and Future Prospects. *Chem. Rev.* **2019**, *119*, 3036−3103.

(3) Green, M. A.; Ho-Baillie, A.; Snaith, H. J. The emergence of perovskite solar cells. *Nat. Photonics* **2014**, *8*, 506−514.

(4) Mitzi, D. B.; Dimitrakopoulos, C. D.; Rosner, J.; Medeiros, D. R.; Xu, Z.; Noyan, C. Hybrid Field-Effect Transistor Based on a Low-Temperature Melt-Processed Channel Layer. *Adv. Mater.* **2002**, *14*, 1772−1776.

(5) Chin, X. Y.; Cortecchia, D.; Yin, J.; Bruno, A.; Soci, C. Lead iodide perovskite light-emitting field-effect transistor. *Nat. Commun.* **2015**, *6*, 7383.

(6) Dou, L.; Yang, Y.; You, J.; Hong, Z.; Chang, W.-H.; Li, G.; Yang, Y. Solution-processed hybrid perovskite photodetectors with high detectivity. *Nat. Commun.* **2014**, *5*, 5404.

(7) Lukosi, E.; Smith, T.; Tisdale, J.; Hamm, D.; Seal, C.; Hu, B.; Ahmadi, M. Methylammonium lead tribromide semiconductors: Ionizing radiation detection and electronic properties. *Nucl. Instrum. Methods Phys. Res., Sect. A* **2019**, *927*, 401−406.

(8) Xu, Q.; Wei, H.; Wei, W.; Chuirazzi, W.; DeSantis, D.; Huang, J.; Cao, L. Detection of charged particles with a methylammonium lead tribromide perovskite single crystal. *Nucl. Instrum. Methods Phys. Res., Sect. A* **2017**, *848*, 106−108.

(9) Zhu, H.; Fu, Y.; Meng, F.; Wu, X.; Gong, Z.; Ding, Q.; Gustafsson, M. V.; Trinh, M. T.; Jin, S.; Zhu, X. Y. Lead halide perovskite nanowire lasers with low lasing thresholds and high quality factors. *Nat. Mater.* **2015**, *14*, 636−642.

(10) Pathak, S.; Sakai, N.; Wisnivesky Rocca Rivarola, F.; Stranks, S. D.; Liu, J.; Eperon, G. E.; Ducati, C.; Wojciechowski, K.; Griffiths, J. T.; Haghighirad, A. A.; Pellaroque, A.; Friend, R. H.; Snaith, H. J. Perovskite Crystals for Tunable White Light Emission. *Chem. Mater.* **2015**, *27*, 8066−8075.

(11) Ling, Y.; Yuan, Z.; Tian, Y.; Wang, X.; Wang, J. C.; Xin, Y.; Hanson, K.; Ma, B.; Gao, H. Bright Light-Emitting Diodes Based on Organometal Halide Perovskite Nanoplatelets. *Adv. Mater.* **2016**, *28*, 305−311.

(12) Era, M.; Morimoto, S.; Tsutsui, T.; Saito, S. Electroluminescent device using two dimensional semiconductor (C6H5C2H4NH3)-2PbI4 as an emitter. *Synth. Met.* **1995**, *71*, 2013−2014.
(13) Eames, C.; Frost, J. M.; Barnes, P. R. F.; O'Regan, B. C.; Walsh, A.; Islam, M. S. Ionic transport in hybrid lead iodide perovskite solar cells. *Nat. Commun.* **2015**, *6*, 7497.
(14) Weller, M. T.; Weber, O. J.; Henry, P. F.; Di Pumpo, A. M.; Hansen, T. C. Complete structure and cation orientation in the perovskite photovoltaic methylammonium lead iodide between 100 and 352 K. *Chem. Commun.* **2015**, *51*, 4180−4183.
(15) Papavassiliou, G. C.; Koutselas, I. B. Structural, optical and related properties of some natural three- and lower-dimensional semiconductor systems. *Synth. Met.* **1995**, *71*, 1713−1714.
(16) Huang, L.-y.; Lambrecht, W. R. L. Electronic band structure, phonons, and exciton binding energies of halide perovskites CsSnCl ${}_{3}$, CsSnBr${}_{3}$, and CsSnI${}_{3}$. *Phys. Rev. B: Condens. Matter Mater. Phys.* **2013**, *88*, 165203.
(17) Matsuishi, K.; Ishihara, T.; Onari, S.; Chang, Y. H.; Park, C. H. Optical properties and structural phase transitions of lead-halide based inorganic−organic 3D and 2D perovskite semiconductors under high pressure. *Phys. Status Solidi B* **2004**, *241*, 3328−3333.
(18) Brivio, F.; Butler, K. T.; Walsh, A.; van Schilfgaarde, M. Relativistic quasiparticle self-consistent electronic structure of hybrid halide perovskite photovoltaic absorbers. *Phys. Rev. B: Condens. Matter Mater. Phys.* **2014**, *89*, 155204.
(19) Rybin, N.; Ghosh, D.; Tisdale, J.; Shrestha, S.; Yoho, M.; Vo, D.; Even, J.; Katan, C.; Nie, W.; Neukirch, A. J.; Tretiak, S. Effects of Chlorine Mixing on Optoelectronics, Ion-Migration and Gamma-ray Detection In Bromide Perovskites. *Chem. Mater.* **2020**, *32*, 1854.
(20) Chung, H.; Jung, S. I.; Kim, H. J.; Cha, W.; Sim, E.; Kim, D.; Koh, W.-K.; Kim, J. Composition-Dependent Hot Carrier Relaxation Dynamics in Cesium Lead Halide (CsPbX3, X = Br and I) Perovskite Nanocrystals. *Angew. Chem., Int. Ed.* **2017**, *56*, 4160−4164.
(21) Yang, Y.; Yan, Y.; Yang, M.; Choi, S.; Zhu, K.; Luther, J. M.; Beard, M. C. Low surface recombination velocity in solution-grown CH3NH3PbBr3 perovskite single crystal. *Nat. Commun.* **2015**, *6*, 7961.
(22) Saidaminov, M. I.; Abdelhady, A. L.; Murali, B.; Alarousu, E.; Burlakov, V. M.; Peng, W.; Dursun, I.; Wang, L.; He, Y.; Maculan, G.; Goriely, A.; Wu, T.; Mohammed, O. F.; Bakr, O. M. High-quality bulk hybrid perovskite single crystals within minutes by inverse temperature crystallization. *Nat. Commun.* **2015**, *6*, 7586.
(23) Piatkowski, P.; Cohen, B.; Javier Ramos, F.; Di Nunzio, M.; Nazeeruddin, M. K.; Grätzel, M.; Ahmad, S.; Douhal, A. Direct monitoring of ultrafast electron and hole dynamics in perovskite solar cells. *Phys. Chem. Chem. Phys.* **2015**, *17*, 14674−14684.
(24) *Optical Techniques for Solid-State Materials Characterization*; Prasankumar, R. P., Taylor, A. J., Eds.; CRC Press: Boca Raton, FL, 2012; pp 291−328.
(25) Yang, Y.; Ostrowski, D. P.; France, R. M.; Zhu, K.; van de Lagemaat, J.; Luther, J. M.; Beard, M. C. Observation of a hot-phonon bottleneck in lead-iodide perovskites. *Nat. Photonics* **2016**, *10*, 53−59.
(26) Righetto, M.; Lim, S. S.; Giovanni, D.; Lim, J. W. M.; Zhang, Q.; Ramesh, S.; Tay, Y. K. E.; Sum, T. C. Hot carriers perspective on the nature of traps in perovskites. *Nat. Commun.* **2020**, *11*, 2712.
(27) Fu, J.; Xu, Q.; Han, G.; Wu, B.; Huan, C. H. A.; Leek, M. L.; Sum, T. C. Hot carrier cooling mechanisms in halide perovskites. *Nat. Commun.* **2017**, *8*, 1300.
(28) Madjet, M. E.; Berdiyorov, G. R.; El-Mellouhi, F.; Alharbi, F. H.; Akimov, A. V.; Kais, S. Cation Effect on Hot Carrier Cooling in Halide Perovskite Materials. *J. Phys. Chem. Lett.* **2017**, *8*, 4439−4445.
(29) Richter, J. M.; Branchi, F.; Valduga de Almeida Camargo, F.; Zhao, B.; Friend, R. H.; Cerullo, G.; Deschler, F. Ultrafast carrier thermalization in lead iodide perovskite probed with two-dimensional electronic spectroscopy. *Nat. Commun.* **2017**, *8*, 376.
(30) Hopper, T. R.; Gorodetsky, A.; Jeong, A.; Krieg, F.; Bodnarchuk, M. I.; Maimaris, M.; Chaplain, M.; Macdonald, T. J.; Huang, X.; Lovrincic, R.; Kovalenko, M. V.; Bakulin, A. A. Hot Carrier Dynamics in Perovskite Nanocrystal Solids: Role of the Cold Carriers, Nanoconfinement, and the Surface. *Nano Lett.* **2020**, *20*, 2271−2278.
(31) Seo, M. A.; Yoo, J.; Dayeh, S. A.; Picraux, S. T.; Taylor, A. J.; Prasankumar, R. P. Mapping Carrier Diffusion in Single Silicon Core−Shell Nanowires with Ultrafast Optical Microscopy. *Nano Lett.* **2012**, *12*, 6334−6338.
(32) Beard, M. C.; Turner, G. M.; Schmuttenmaer, C. A. Transient photoconductivity in GaAs as measured by time-resolved terahertz spectroscopy. *Phys. Rev. B: Condens. Matter Mater. Phys.* **2000**, *62*, 15764−15777.
(33) Gershenzon, M.; Mikulyak, R. M. Radiative Pair Recombination and Surface Recombination in GaP Photoluminescence. *Appl. Phys. Lett.* **1966**, *8*, 245−247.
(34) Sabbah, A. J.; Riffe, D. M. Measurement of silicon surface recombination velocity using ultrafast pump−probe reflectivity in the near infrared. *J. Appl. Phys.* **2000**, *88*, 6954−6956.
(35) Yin, W.-J.; Shi, T.; Yan, Y. Unique Properties of Halide Perovskites as Possible Origins of the Superior Solar Cell Performance. *Adv. Mater.* **2014**, *26*, 4653−4658.
(36) Hoffman, C. A.; Jarašiūnas, K.; Gerritsen, H. J.; Nurmikko, A. V. Measurement of surface recombination velocity in semiconductors by diffraction from picosecond transient free-carrier gratings. *Appl. Phys. Lett.* **1978**, *33*, 536−539.
(37) Shi, D.; Adinolfi, V.; Comin, R.; Yuan, M.; Alarousu, E.; Buin, A.; Chen, Y.; Hoogland, S.; Rothenberger, A.; Katsiev, K.; Losovyj, Y.; Zhang, X.; Dowben, P. A.; Mohammed, O. F.; Sargent, E. H.; Bakr, O. M. Low trap-state density and long carrier diffusion in organolead trihalide perovskite single crystals. *Science* **2015**, *347*, 519−522.
(38) Ruzicka, B. A.; Werake, L. K.; Samassekou, H.; Zhao, H. Ambipolar diffusion of photoexcited carriers in bulk GaAs. *Appl. Phys. Lett.* **2010**, *97*, 262119.
(39) Zhao, H. Temperature dependence of ambipolar diffusion in silicon on insulator. *Appl. Phys. Lett.* **2008**, *92*, 112104.

https://dx.doi.org/10.1021/acs.jpclett.0c02243
J. Phys. Chem. Lett. 2020, 11, 8430−8436